



Observation of Topological Transmission in Terahertz Domino Waveguide Array

Pan Hu, Lin Chen , *Member, IEEE*, Alexander Pavlovich Shkurinov, Yiming Zhu , *Senior Member, IEEE*, and Songlin Zhuang

Abstract—In this article, we propose on-chip terahertz (THz) domino waveguide array structures that can enable the topological effect and enhance the robustness of THz transmission. THz topological effect (include topologically protected edge states and binding states) is excited by constructing kink and antikink structures in designed domino waveguide arrays. Furthermore, the robustness of topological waveguide arrays is successfully demonstrated. The topological transmission effects have been experimentally demonstrated using scanning near-field THz microscopy. Our study provides a new approach to study the topological photonic transport of waveguide arrays in the THz regime and has potential application in THz-integrated circuit.

Index Terms—Domino plasmons, terahertz (THz), topological photonics, waveguide array.

I. INTRODUCTION

TERAHERTZ (THz) waves are located between microwave and infrared waves (0.1–10 THz) [1], [2], [3]. They show some unique characteristics, such as fingerprint spectrum identification [4], nondestructive detection [5], and broadband 6G communication [6], and thus, have recently paid much more attention for both mechanisms and applications. However, most THz systems are composed of bulky and discrete components, including coupler, beam splitter, waveguides, and lenses [7], [8], [9], [10], [11], [12]. An on-chip integration platform is required to reduce the size of the components. This on-chip

Manuscript received 31 October 2022; revised 16 March 2023, 4 April 2023, and 21 April 2023; accepted 6 May 2023. Date of publication 11 May 2023; date of current version 3 July 2023. This work was supported in part by the Basic Science Center Project of the National Natural Science Foundation of China under Grant 61988102, in part by the National Natural Science Foundation of China under Grant 62275157, in part by Shanghai Shuguang Program, China, under Grant 18SG44, and in part by 111 Project under Grant D18014. (Corresponding author: Lin Chen.)

Pan Hu, Yiming Zhu, and Songlin Zhuang are with the Shanghai Key Lab of Modern Optical System, University of Shanghai for Science and Technology, Shanghai 200093, China (e-mail: hupan13865117217@163.com; ymzhu@usst.edu.cn; slzhuang@yahoo.com).

Lin Chen is with the Shanghai Key Lab of Modern Optical System, University of Shanghai for Science and Technology, Shanghai 200093, China, and also with the Shanghai Institute of Intelligent Science and Technology, Tongji University, Shanghai 200092, China (e-mail: linchen@usst.edu.cn).

Alexander Pavlovich Shkurinov is with the Faculty of Physics and International Laser Center, Lomonosov Moscow State University, 119991 Moscow, Russia (e-mail: ashkurinov@physics.msu.ru).

This article has supplementary material provided by the authors and color versions of one or more figures available at <https://doi.org/10.1109/TTHZ.2023.3275270>.

Digital Object Identifier 10.1109/TTHZ.2023.3275270

integration platform is also defined as THz-integrated circuit (IC) [13], [14], [15], which is indispensable toward the practical use in various fields. The low-loss waveguides on chip are the most fundamental and key components for the development of THz ICs. Various waveguides on a thin planar platform had been fully discussed, such as transmission line [16], [17], [18] and silicon photonic crystals (PC) [19], [20], [21]. THz transmission lines are 1-D transmission waveguide and can be easily fabricated by the conventional electronics and photonics' technologies, but they suffered from large ohmic loss induced by metals at THz frequencies. Silicon PC slabs consisting of a 2-D lattice of air holes demonstrate the strong electromagnetic confinement due to the existence of photonic band gap. Such PC waveguides and silicon waveguides using total internal reflections [22], [23], [24], [25], [26] can also realize a low-loss waveguide because the silicon absorption can be managed by controlling the doped carrier density. They have several advantages.

- 1) Modal fields can be confined into a subwavelength-width core.
- 2) It is proved to be compact, for instance, the lateral periodicity of the PC is about 25% of a free-space wavelength at about 0.3 THz [19].
- 3) It is monolithic because the entire structure is fabricated from a single silicon wafer.
- 4) It is versatile and can integrate various functions, such as frequency-division multiplexer [20], antenna array [21], and topological on chip communication [27].

We noticed that the THz wave was commonly coupled into PC waveguides by hollow metallic waveguide and tapered structure. And, PC waveguides were measured by using a continuous wave electronic source, which was produced by combining a millimeter-wave signal generator and multiplier and showed limited bandwidth (for instance, 0.28–0.39 THz range in [19]). To cover wideband frequency range (for instance, 0.1–1.5 THz), double or triple frequency conversion should be prepared. Typical tripler conversion efficiency of multiplier is low (1.5% for output frequency range 0.5–0.75 THz and 0.1%–0.7% for output frequency range 1.1–1.6 THz) [28], resulting in low output power. Meanwhile, broadband THz time domain spectroscopy (TDS) system is widely used in THz field. Therefore, exploring alternative robust THz waveguides in combination with broadband THz TDS system is necessary to achieve THz IC with selected operation frequency.

Domino waveguide, which consists of a chain of periodic metallic domino-like pieces on top of a metallic surface [29], is an excellent candidate for the building of compact THz ICs. Domino waveguides have the same features as PC waveguides.

- 1) It carries subwavelength transverse cross-sectional localization.
- 2) It is planar, monolithic, and easily manufactured.
- 3) It is versatile for the design of key functional devices with small absorption and bend losses [30].

The flexibility and versatility of domino waveguides had already been demonstrated through the implementation of a variety of functional devices, such as THz coupler [31], switch [32], beam splitter [30], wavelength-division multiplexing [33], and logic gate structure devices [34]. More importantly, the THz wave can be coupled into domino waveguides by integrated with tapered grating on a single silicon wafer. And domino waveguides can be successfully measured by using a THz scanning near-field THz microscopy with a broadband photoconductive emission antenna and a probe [30]. In this work, the THz domino waveguides array is fully investigated to further expand the applications of domino platform. To the best of our knowledge, it is the first time that the THz topological transport has been implemented on the coupled domino waveguides array [29]. First, we analyze the dispersion properties of two domino waveguides and the coupling properties between two waveguides. Then, we develop the Su–Schrieffer–Heeger (SSH) model [35], [36], [37], [38] for the domino waveguides array structure and derive the Hamiltonian matrix by coupling-mode theory and the Schrödinger equation. Third, by using the domino waveguide array parameters and designing the kink and antikink structures [39], we have successfully excited the THz topologically protected edge states and binding states and verified the robustness of both topologies by introducing structural deviation degree. The topological transmission of our domino platform has a significant role in both foundation and application. Fundamentally, the domino waveguides array provides macroscopic THz platform analogs of such important quantum phenomena (the topological phases) in the condensed matters without requiring special synthetic media with subwavelength controllability. In application, our work realized that the topological protection is introduced into THz IC, which can enhance the robustness of THz signal integrity with defects and disorders, i.e., significant features in THz communications [13], [14], [15].

II. DESIGN OF THz 1-D TOPOLOGICAL PHOTONIC CHIP

Fig. 1 shows a schematic of implementing topological effect in THz 1-D domino waveguide array. The structure is divided into three parts: the excitation region, the energy focus region, and the energy transmission region. THz spoof surface plasmonic polariton [40], [41], [42], [43], [44] is excited by the curved holes array. The excited domino plasmon is focused through periodic-decreasing fan funnel waveguides and finally transmitted through the transmission region. The upper left inset of Fig. 1 is the design of the antikink and kink structures. The single domino waveguide structure is shown in the lower right inset of Fig. 1.

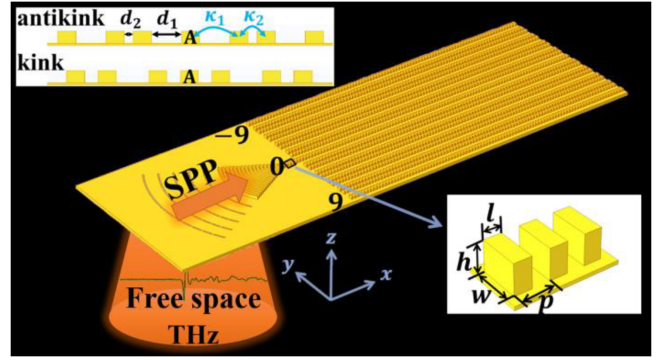


Fig. 1. Schematic of implementing THz topologically protected edge states in the 1-D domino waveguide array. The upper left inset is the antikink and kink structures [d (d_1 and d_2) represents the waveguide spacing, κ (κ_1 and κ_2) is the coupling coefficient between the waveguides, and A represents the central waveguide of the input energy]. The lower right inset is detailed domino waveguide structure, where $w = 120 \mu\text{m}$, $p = 100 \mu\text{m}$, $h = 80 \mu\text{m}$, and $l = 50 \mu\text{m}$. We number the waveguide array along the y -axis from positive to negative direction as $-9, \dots, 9$.

We choose the parameters of the single domino structure as $w = 120 \mu\text{m}$, $p = 100 \mu\text{m}$, $h = 80 \mu\text{m}$, and $l = 50 \mu\text{m}$. The eigenmode solver of the commercial software CST Microwave Studio is used to analyze the dispersion curves of the odd mode (k_{ssppo}) and even mode (k_{ssppe}) with different waveguide spacing d , as shown in Fig. 2(a). Based on the equation $k_{\text{sspp}} = \theta * \pi / (180 * p)$, the values of k_{sspp} were obtained, where θ is the variation in x -direction. Here, the k_{sspp} is equivalent to the propagation constant β in the waveguide.

Within the first Brillouin zone, the k_{sspp} of the domino waveguide mode became larger than the light line (black dotted line) with increasing frequency, which means that the surface with pillars possesses good field confinement ability. For the odd mode, the cutoff frequency increases with the increase of d . For the even mode, the cutoff frequency decreases with the increase of d . The upper left inset of Fig. 2(a) shows the normalized electric field distribution of the two modes with $d = 60 \mu\text{m}$ at 0.5 THz. To obtain the relation between the different waveguide spacing d and the coupling coefficients κ , we use the supermode theory to analyze. The difference of the propagation constants k_{sspp} for two supermodes causes the phase difference. When the phase difference reaches π , the energy is coupled from one waveguide to another, with its length called L_c . The relationship between coupling length L_c and the coupling coefficients κ is $\kappa L_c = \pi / 2$, where $\kappa = (k_{\text{ssppe}} - k_{\text{ssppo}}) / 2$. We also plot the relationship between waveguide spacing d and the coupling coefficient κ , as shown in Fig. 2(b). By using the supermode theory, it can be found that the coupling coefficient decreases with the increasing waveguide spacing. These results will be used in the following THz topological domino waveguide design.

THz wave is commonly coupled into the PC waveguides from the waveguide port by employing the near-field coupling techniques [19]. However, such near-field coupling techniques cannot be employed into the domino waveguide due to the momentum mismatch between free-space THz wave vector and domino surface plasmons wave vector. The methods on the

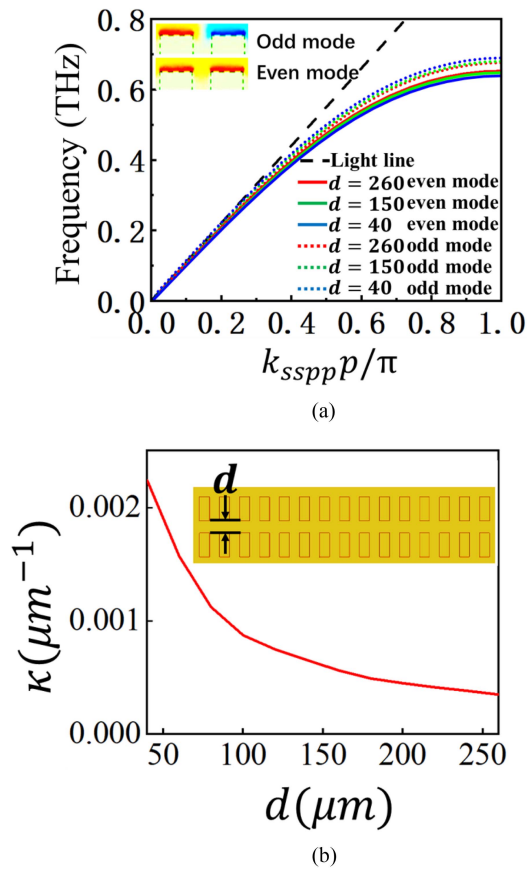


Fig. 2. (a) Dispersion relation of odd and even modes for waveguides with varying d . The upper left inset shows the normalized electric field distribution of the two modes with $d = 60 \mu\text{m}$ at 0.5 THz. (b) Coupling coefficients κ as a function of gap d .

excitation of THz domino surface plasmons that can achieve the momentum match are generally based on prism coupling or grating coupling [45]. Compared with prism coupling in which the existence of bulk prism does not benefit to integration, the grating coupling with a gradually reduced width next to the grating can convert more free-space THz waves to domino surface plasmons at the on-chip integration platform without any bulk prism usage.

The excited domino plasmon is coupled to the waveguide through a fan funnel consisted of a period-reduced column. Both the excited hole arrays and a funnel-shaped array of metal columns have the ability to focus the energy on a strong point with a subwavelength width. The schematic of the arc-shaped curved hole array excitation and the fan-shaped coupling region, as well as the scanning electron microscopy (SEM) image consisting coupling and focusing regions, is shown in Fig. 3(a)–(c). The radii of the innermost and outermost layers of the curved hole array are $2220 \mu\text{m}$ and $3820 \mu\text{m}$, respectively. The width of each hole array is $40 \mu\text{m}$, the period along the radial direction is $400 \mu\text{m}$, and the center corner of the curved hole is 60° . The curved hole arrays are divided into smaller holes by metal strips with a spacing of $50 \mu\text{m}$ and a center angle of 5° . The radial period between the arc waveguides is $100 \mu\text{m}$, and each array width is $50 \mu\text{m}$. To evaluate the coupling efficiency of the

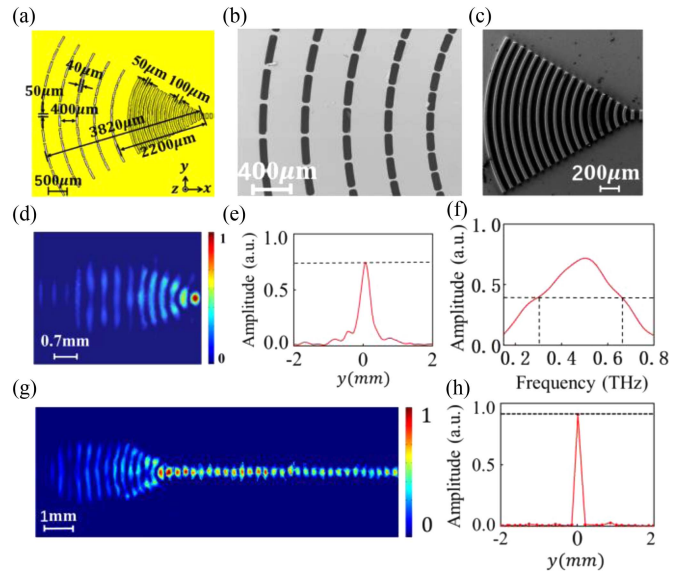


Fig. 3. (a) Schematic of the coupling and focused regions. (b) and (c) SEM image of the fabricated arc-shaped curved hole array excitation region as well as the fan-shaped coupling region. (d) Simulated electric field distribution of (a). (e) Amplitude of the electric field at 0.5 THz for the output port of coupling region in (a). (f) Amplitude at output port of coupling region as a function of operation frequency. (g) Electric field distributions at 0.5 THz corresponding to the single root waveguide. (h) Output port amplitude distribution for the single domino waveguide.

grating coupler, we numerically obtained the output electric field amplitude of the waveguide at the end of the coupling region at 0.5 THz, as shown in Fig. 3(d) and (e). The coupling efficiency is about 73% at 0.5 THz. We also obtained the coupling efficiency of the grating coupler with respect to the operation frequency, as shown in Fig. 3(f). At broadband frequency range 0.3–0.66 THz, the coupling efficiency of the grating coupler can achieve larger than 40%.

To verify the focusing power of this structure, we simulated the electric field distribution of a single domino waveguide, as shown in Fig. 3(g). The results demonstrate that the electric field is well focused on the single domino waveguide, which is also clearly proved by the output port amplitude distribution in Fig. 3(h) (normalized by input port amplitude at the output port of coupling region).

The above result in Fig. 3(h) neglects actual metallic loss in simulation. Actually, a thin gold film was coated on the silicon wafer. So, the ohmic loss of the metal should be taken into account. For single domino waveguide [see Fig. 4(a)], Fig. 4(b) shows the propagation length l as a function of operation wavelength by considering the ohmic loss of the metal. Here, $l = (2\text{Im}(k))^{-1}$, where $\text{Im}(k)$ is the imaginary part of the propagation constant of domino surface plasmons. As operation wavelength increases from cutoff wavelength (0.47 mm), propagation length increases and the dispersion curve approaches the light line. For $\lambda = 0.6 \text{ mm}$ (0.5 THz), $h = 0.8p$, $w = 1.2p$, and $p = 100 \mu\text{m}$, the propagation length is about 20λ or 12 mm when amplitude reduces to $0.368 (1/e)$. The propagation length is larger than the size of the chips in this work. The simulated power propagation losses of the single straight waveguide are

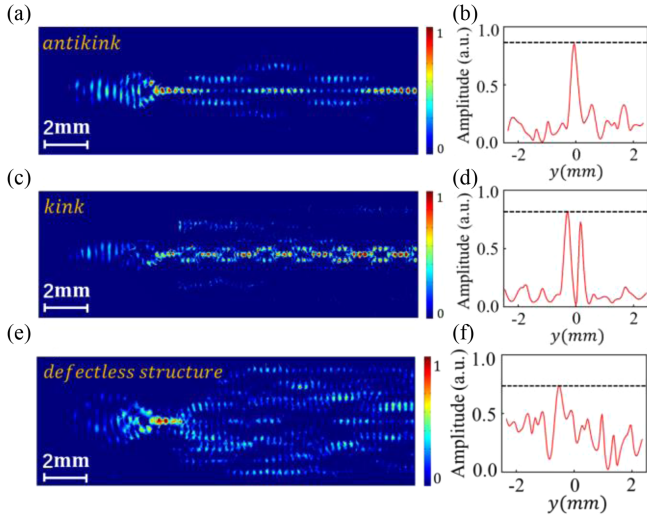


Fig. 7. Three-dimensional simulation results at the 0.5 THz frequency. (a) Electric field distributions corresponding to the antikink structure. (b) Amplitude distribution of the output port for the antikink structure. (c) Electric field distributions corresponding to the kink structure. (d) Amplitude distribution of the output port for the kink structure. (e) Electric field distributions corresponding to the defectless structure. (f) Amplitude distribution of the output port for the defectless structure.

waveguide. The amplitude with loss of metal is 0.48, indicating that the power propagation loss is 0.64 dB/mm. For the kink structure, two binding modes were excited, which are located outside the body band of the band structure, and both have a strong distribution over the central waveguide. Thus, center waveguide input excites both binding modes. Meanwhile, due to their different mode constants, the THz domino plasmon transmission presents a beating effect. The amplitude distribution at the output port of the kink structure is shown in Fig. 7(d). Since the electric field fluctuates between right to the two subcentral waveguides, most of the energies are localized in these two waveguides. The amplitude with loss of metal is 0.36/0.32, indicating that the power propagation loss is 0.89/0.99 dB/mm. The electric field distributions of these two structures correspond exactly to the theoretical analysis [see Fig. 6(a) and (b)]. To highlight the topological transport behavior of the antikink and kink structures, we designed equidistantly spaced ($d_1 = d_2 = 100 \mu\text{m}$) waveguide structures for contrast. The structure without introducing a topology belongs to the defectless structures. It is found that the electric field transports throughout the waveguide and presents an irregular distribution, as shown in Fig. 7(e). The corresponding output port amplitude distribution is shown in Fig. 7(f). The amplitude with loss of metal is 0.2, indicating that the power propagation loss is 1.4 dB/mm.

IV. ROBUSTNESS OF THE TOPOLOGICAL STRUCTURE

A. Antikink Structure

To verify the robustness of the topology, structural deviation degree φ is introduced in the waveguide spacing d_1 . Change d_1 can directly change the coupling coefficients between the waveguides. For both structures, we introduce different φ by changing d_1 . For the antikink structure, most energy remains

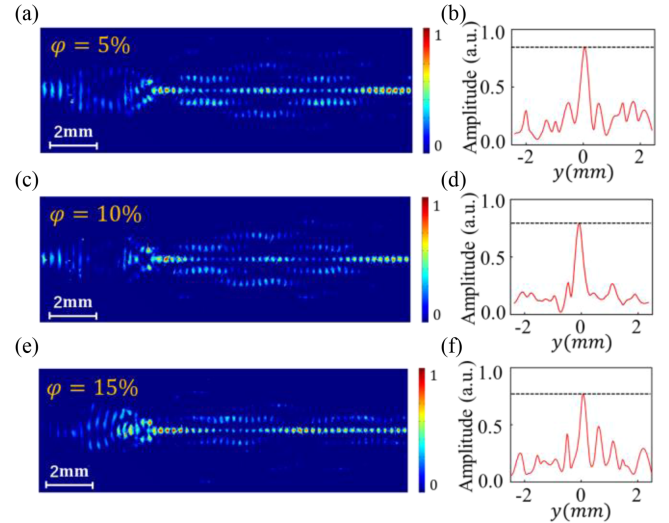


Fig. 8. For the antikink structure, the 3-D simulation results with different structural deviation degrees φ are introduced at 0.5 THz frequency. (a) Electric field distributions under the 5% deviation degree. (b) Amplitude distribution of the output for 5% deviation degree. (c) Electric field distributions under the 10% deviation degree. (d) Amplitude distribution of the output port for the 10% deviation degree. (e) Electric field distributions under the 15% deviation degree. (f) Amplitude distribution of the output port for the 15% deviation degree.

confined to the central waveguide when introduced 5% and 10% structural deviation degree, which shows good robustness, as shown in Fig. 8(a) and (c). When 15% of the φ is introduced, most energy is still limited to the central waveguide, although the subcentral waveguide also has a partial energy output [see Fig. 8(e)]. The amplitude distribution of the output port corresponding to the simulation results under these three different φ is shown in Fig. 8(b), (d), and (f). For antikink structures, it is well robust to structural deviation and fits with topological features. The amplitude with loss of metal for φ of 5%, 10%, and 15% is 0.42, 0.38, and 0.32, indicating that the power propagation loss is 0.75 dB/mm, 0.84 dB/mm, and 0.99 dB/mm, respectively. The robustness of the antikink structure with respect to dimer number N can also be found in the supplementary material [46].

B. Kink Structure

For the kink structure, we verify its robustness in the same way, as shown in Fig. 9. By introducing different structural deviation degrees φ on the basis of this structure, we can find that the energy still oscillates around the central waveguide from the normalized electric field distribution of the simulation, but some of the energy is coupled to other waveguides. From the normalized electric field distribution of the output port, it can be seen that after the introduction of different structural deviation degrees φ , the energy distribution in the whole waveguide is not obvious, although the subcentral waveguide has two higher peaks. It can be found that the robustness decreases with the increase of φ . Because in kink structure, only two binding modes are excited, which are not in the band gap, and they do not have good robustness. This is completely consistent with the theoretical analysis. The amplitude with loss of metal for φ of 5%, 10%, and 15% is 0.3/0.26, 0.28/0.24, and 0.22/0.18,

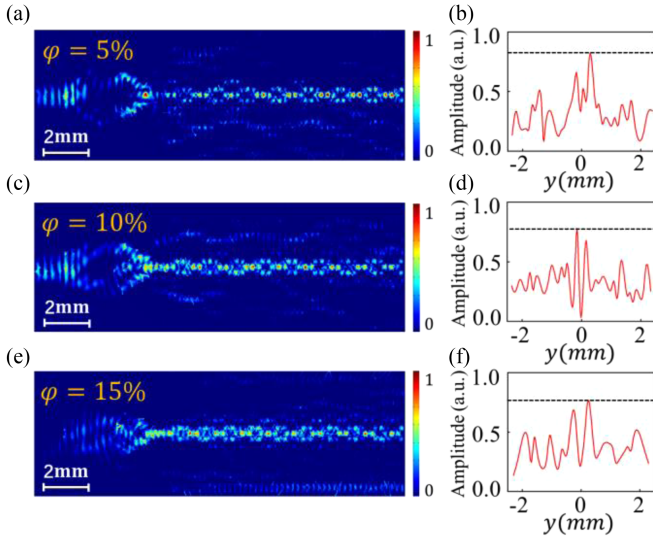


Fig. 9. For the kink structure, 3-D simulation results with different structural deviation degrees φ are introduced at 0.5 THz frequency. (a) Electric field distributions under the 5% deviation degree. (b) Amplitude distribution of the output port for the 5% deviation degree. (c) Electric field distributions under the 10% deviation degree. (d) Amplitude distribution of the output port for the 10% deviation degree. (e) Electric field distributions under the 15% deviation degree. (f) Amplitude distribution of the output port for the 15% deviation degree.

indicating that the power propagation loss is 1.05/1.17 dB/mm, 1.11/1.24 dB/mm, and 1.32/1.49 dB/mm, respectively.

To demonstrate the robustness of waveguiding by a single topological defect in such domino waveguide platform, we give the fluctuation for x and y directions for the central waveguide and evaluate the performance improved by introducing the periodic structures. First, the propagation performance was studied by adding the curving central waveguide in the antikink structure [see Fig. 10(a)], which means the inter- and intradimer coupling coefficient is not equal at the interface between red dimer chain and blue dimer chain. Simulation result shows that the electric field energy is still found in the center waveguide without dramatically degrading the signal integrity because the structure is still topologically protected, as shown in Fig. 10(a) and (b). Second, we gave the fluctuation for x directions for the central waveguide, which is achieved by extracting some pillars in the central domino waveguide and arrange some pillars to randomly deviate from center line. We compared the transmission performances of topological waveguide to single-row domino guide by introducing the same defects, as shown in Fig. 10(c) and (e). The results show that the THz wave can successfully propagate to the end of central waveguide by exciting antikink mode [see Fig. 10(d)], while the energy with domino plasmonic mode in single-row guide is reduced significantly, as shown in Fig. 10(f) and (g).

All the above results in an unambiguous way proved the robustness of the system by a single topological defect in a domino waveguide platform.

V. EXPERIMENT

A two-step process is employed to fabricate the high-quality domino array structure. First, optical lithography and deep reactive ion etching techniques are used to obtain the basic

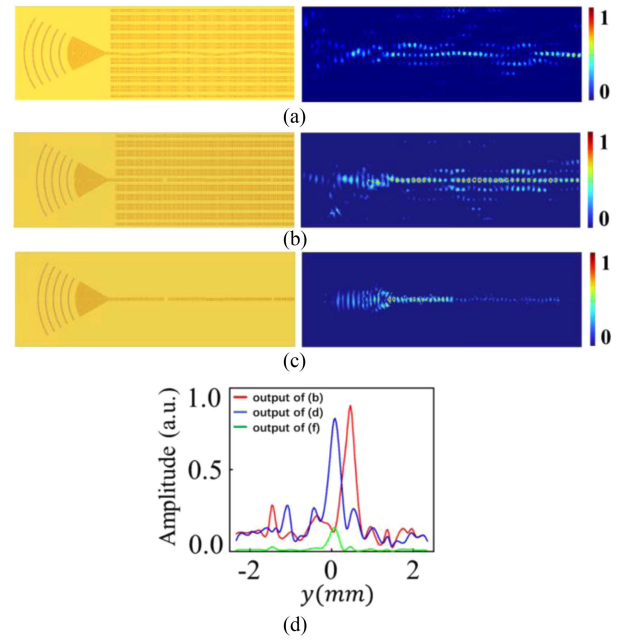


Fig. 10. (a) Schematic of antikink structure with central curving waveguide. (b) Electric field distributions of (a). (c) Schematic of the antikink structure by extracting some pillars in the central domino waveguide and arrange some pillars to randomly deviate from center line. (d) Electric field distributions of (c). (e) Schematic of the single domino waveguide by introducing the same defects as (c). (f) Electric field distributions of (e). (g) Amplitude of the electric field of the output ports in (b), (d), and (f).

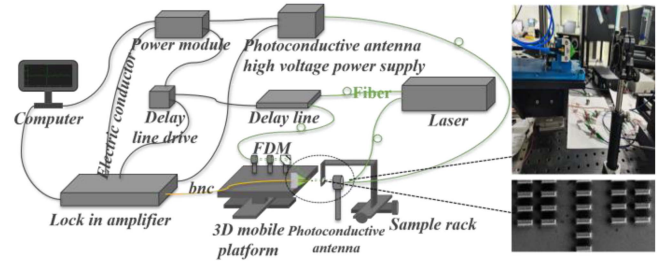


Fig. 11. Illustration of the experimental setup. The upper right inset is the experimental process. The lower right inset is the SEM image of the energy transmission region.

waveguide structure on a 4-in silicon wafer, where the excitation area is etched into a through-hole. In the second process, a 200-nm-thick gold film metallization of the chips is then conducted in a gold sputter coater. The thickness of gold is selected based on the penetration depth of the THz wave in the metal.

We experimentally verify this phenomenon by scanning near-field THz microscopy, which has been used in our lab for near-field detection of THz functional devices [47], [48], [49]. The schematic of the system is shown in Fig. 11. The light source is a femtosecond fiber laser with a central wavelength of 1560 nm. The laser output port is divided into two beams, detection light and pump light. The beam used for detection passes through the optical fiber and radiates the laser through the frequency doubling module to the metal junction of the microprobe. The probe is based on GaAs grown at low temperatures. Since the laser at the wavelength of 1560 nm cannot excite the carrier in GaAs, it is necessary to convert it from 1560 to 780 nm. The pump light is connected to the photoconductive emission

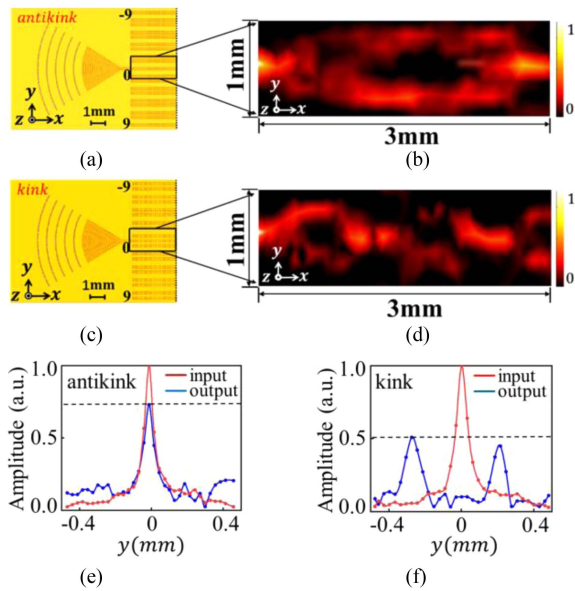


Fig. 12. Experimental results. (a) Schematic representation of the antikink structure. (b) Electric field distributions of the boxed sections in Fig. (a). (c) Schematic representation of the kink structure. (d) Electric field distributions of the boxed sections in Fig. (c). (e) Amplitude distributions at the output port of the antikink structure in Fig. (b). (f) Amplitude distributions at the output port of the kink structure in Fig. (d). All the propagation lengths are 3 mm.

antenna through the optical fiber delay line, which is two parallel metal wires embedded on the surface of the semiconductor substrate material. Then, the photoconductive emission antenna is exposed to the pump light, producing THz radiation. The domino plasmon is generated after the THz wave is input into the excitation region of the sample. Since the boundary surface of the waveguide is an evanescent field, the probe needs to be so close to the sample. Then, move the probe in the x - y -direction for point-by-point scanning. The probe sends the acquired time-domain signal to the computer by using the current signal amplifier and the phase-lock amplifier, and then obtain the near-field image by the commercial software MATLAB.

We placed the sample vertically on the sample holder and used the CCD camera to observe the distance between the probe and the sample. We controlled the distance about $100 \mu\text{m}$ between the probe and the sample. The probe is mounted on a 2-D translation detector and moved in the x -directions in $100 \mu\text{m}$ steps and y -directions in $30 \mu\text{m}$ steps [48]. For the actual scanning region of our system, we chose a range of $3 \times 1 \text{ mm}$ for scanning. For the antikink structure, the scan range is shown in the boxed area of Fig. 12(a). The scan results indicate that the energy is mostly concentrated in the central waveguide. When transmitting about one-third of the distance, the energy moves to the upper and lower waveguide. Despite the energy transition to the upper and lower waveguide, it returns to the central waveguide when transmitting two-thirds of the distance, as shown in Fig. 12(b). This transmission mode is achieved because the energy is input from the waveguide at the center of the interface, which successfully matches the topological defect mode. The topological defect mode is topologically protected, thus enabling robust transmission at the center.

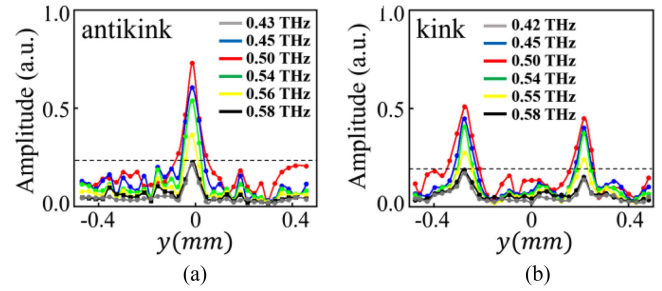


Fig. 13. Measured amplitude of the electric field at the output ports of (a) antikink structure and (b) kink structure by extracting corresponding frequency.

To more precisely observe the amplitude distribution at the output port of the antikink structure, we plotted the amplitude distribution of the input and output ports of the waveguide arrays, as shown in Fig. 12(e). Here, we normalized input THz wave instead of output THz wave. The power propagation loss of the antikink structure is 0.91 dB/mm . It can be found that a significant peak appears at the central position, while the energy distribution at other positions is significantly low. The experimental results are perfectly consistent with the simulated results.

For the kink structure, the scan range is shown in the box in Fig. 12(c). The scan results indicate that no energy is distributed at the central waveguide when the energy fluctuates to the upper and lower waveguide, as shown in Fig. 12(d). In our experiments, the energy oscillates three times and outputs at the port in the form of oscillation. Through the above topological analysis, the energy of the subcentral waveguide belongs to the two binding modes in the band diagram. They are located outside the body band of the band structure. Thus, a single waveguide input at the center will excite both binding modes simultaneously, and the electric field transport presents a beat effect due to their different mode constants.

To precisely observe the amplitude distribution at the output port of the kink structure, we also plotted the amplitude distribution of the input and output ports of the waveguide arrays, as shown in Fig. 12(f), and the power propagation loss of the kink structure is 1.93 dB/mm (left peak) and 2.31 dB/mm (right peak). Two distinct peaks can be found approximately 0.4 mm away from the central waveguide. The position where the central waveguide is located has a very low energy. The experimental results are perfectly consistent with the simulated results.

We also analyzed the amplitude of the electric field at the output port of the antikink and kink structures when propagation length is 3 mm by extracting corresponding frequency. The results are shown in Fig. 13. The dynamic range of output amplitude is beyond 0.2 – 0.73 for antikink structure and 0.2 – 0.52 for kink structure. The operation bandwidth of the antikink structure is about 150 GHz (0.43 – 0.58 THz) in the dynamic range and the operation bandwidth of the kink structure is about 160 GHz (0.42 – 0.58 THz), as shown in Fig. 13(a) and (b), respectively.

VI. CONCLUSION

In summary, we realized the THz topologically protected edge states and binding states by constructing both the kink and

antikink structures in the THz domino waveguides array. We analyzed the dispersion and coupling properties of waveguides by supermode theory. Through theoretical analysis, the THz topological defect mode appears at the center of the energy band, and the central transmission of the topological defect mode in the waveguide array is also observed from the simulation results. To verify the robustness of this topology, we perform a simulation analysis by introducing different structural deviation degrees, which show that the antikink structures are competent to against the structural deviation. The experimental results verified such topological phase features. Our work introduces topological photonics into THz spectral with domino waveguides array platform. On one side, this platform and its near-field measurements can easily demonstrate many quantum phenomena, which are found first in the condensed matters. On the other side, THz signals manipulated in circuits maintain much more integrity and robustness with fabrication imperfect, sample defects, or period disorders by introducing topological protection state.

ACKNOWLEDGMENT

The authors would like to thank Prof. Q. Cheng of the University of Shanghai for Science and Technology for his theoretical guidance and Associate Professor Y. Li and Dr. M. Yuan of Tianjin University for their experimental guidance.

REFERENCES

- [1] C. Sirtori, "Bridge for the terahertz gap," *Nature*, vol. 417, no. 6885, pp. 132–133, 2002.
- [2] B. Ferguson and X.-C. Zhang, "Materials for terahertz science and technology," *Nature Mater.*, vol. 1, no. 1, pp. 26–33, 2002.
- [3] D. M. Mittleman, "Perspective: Terahertz science and technology," *J. Appl. Phys.*, vol. 122, no. 23, 2017, Art. no. 230901.
- [4] Y. C. Shen et al., "Detection and identification of explosives using terahertz pulsed spectroscopic imaging," *Appl. Phys. Lett.*, vol. 86, no. 24, 2005, Art. no. 241116.
- [5] F. Xu, Q. D. D. Mu, L. J. Li, D. Yang, and B. Xia, "Nondestructive evaluation of rubber composites using terahertz time domain spectroscopy," *Fibres Textiles Eastern Europe*, vol. 26(1(127)), pp. 67–72, 2018.
- [6] T. Nagatsuma, G. Ducournau, and C. C. Renaud, "Advances in terahertz communications accelerated by photonics," *Nature Photon.*, vol. 10, no. 6, pp. 371–379, 2016.
- [7] L. Chen et al., "Observation of electromagnetically induced transparency-like transmission in terahertz asymmetric waveguide-cavities systems," *Opt. Lett.*, vol. 38, no. 9, pp. 1379–1381, 2013.
- [8] L. Chen et al., "Tunable phase transition via radiative loss controlling in a terahertz attenuated total reflection-based metasurface," *IEEE Trans. Terahertz Sci. Technol.*, vol. 9, no. 6, pp. 643–650, Nov. 2019.
- [9] L. Chen et al., "Mode splitting transmission effect of surface wave excitation through a metal hole array," *Light, Sci. Appl.*, vol. 2, no. 3, 2013, Art. no. e60.
- [10] B. Lv et al., "All-dielectric metasurface-based quad-beam splitter in the terahertz regime," *IEEE Photon. J.*, vol. 12, no. 5, Oct. 2020, Art. no. 4601410.
- [11] Q. Cheng et al., "Achromatic terahertz airy beam generation with dielectric metasurfaces," *Nanophotonics*, vol. 10, no. 3, pp. 1123–1131, 2021.
- [12] K. Xi et al., "Terahertz airy beam generated by Pancharatnam-Berry phases in guided wave-driven metasurfaces," *Opt. Express*, vol. 30, no. 10, pp. 16699–16711, 2022.
- [13] A. Kumar et al., "Phototunable chip-scale topological photonics: 160 Gbps waveguide and demultiplexer for THz 6G communication," *Nature Commun.*, vol. 13, no. 1, 2022, Art. no. 5404.
- [14] A. Kumar et al., "Active ultrahigh-Q (0.2×10^6) THz topological cavities on a chip," *Adv. Mater.*, vol. 34, no. 27, 2022, Art. no. 2202370.
- [15] A. Kumar, M. Gupta, and R. Singh, "Topological integrated circuits for 5G and 6G," *Nature Electron.*, vol. 5, no. 5, pp. 261–262, 2022.
- [16] L. Chen et al., "Terahertz time-domain spectroscopy and micro-cavity components for probing samples: A review," *Front. Inf. Technol. Electron. Eng.*, vol. 20, no. 5, pp. 591–607, 2019.
- [17] J. Zhou et al., "Terahertz on-chip sensing by exciting higher radial order spoof localized surface plasmons," *Appl. Phys. Express*, vol. 13, no. 1, 2019, Art. no. 012014.
- [18] K. Tsuruda et al., "Ultralow-loss photonic-crystal waveguides for gigabit terahertz-wave communications," in *Proc. IEEE Int. Topical Meeting Microw. Photon.*, 2013, pp. 9–12.
- [19] K. Tsuruda, M. Fujita, and T. Nagatsuma, "Extremely low-loss terahertz waveguide based on silicon photonic-crystal slab," *Opt. Express*, vol. 23, no. 25, pp. 31977–31990, 2015.
- [20] W. Withayachumnankul, M. Fujita, and T. Nagatsuma, "Integrated silicon photonic crystals toward terahertz communications," *Adv. Opt. Mater.*, vol. 6, no. 16, 2018, Art. no. 1800401.
- [21] W. Withayachumnankul, R. Yamada, M. Fujita, and T. Nagatsuma, "All-dielectric rod antenna array for terahertz communications," *Appl. Phys. Lett. Photon.*, vol. 3, no. 5, 2018, Art. no. 051707.
- [22] W. Gao et al., "Effective-medium-cladded dielectric waveguides for terahertz waves," *Opt. Express*, vol. 27, no. 26, pp. 38721–38734, 2019.
- [23] D. Headland, W. Withayachumnankul, X. Yu, M. Fujita, and T. Nagatsuma, "Unclad microphotonics for terahertz waveguides and systems," *J. Lightw. Technol.*, vol. 38, no. 24, pp. 6853–6862, Dec. 2020.
- [24] M. Verstuyft et al., "Short bends using curved mirrors in silicon waveguides for terahertz waves," *Opt. Express*, vol. 30, no. 5, pp. 6656–6670, 2022.
- [25] R. Koala et al., "Ultra-low-loss and broadband all-silicon dielectric waveguides for WR-1 band (0.75–1.1 THz) modules," *Photonics*, vol. 9, no. 8, 2022, Art. no. 515.
- [26] A. Rivera-Lavado et al., "Contactless RF probe interconnect technology enabling broadband testing to the terahertz range," *IEEE Trans. Terahertz Sci. Technol.*, vol. 13, no. 1, pp. 34–43, Jan. 2023.
- [27] Y. Yang et al., "Terahertz topological photonics for on-chip communication," *Nature Photon.*, vol. 14, no. 7, pp. 446–451, 2020.
- [28] "The user guide manual in," 2014. [Online]. Available: www.mtinstruments.com
- [29] D. Martín-Cano et al., "Domino plasmons for subwavelength terahertz circuitry," *Opt. Express*, vol. 18, no. 2, pp. 754–764, 2010.
- [30] Y. Zhang et al., "Terahertz spoof surface-plasmon-polariton subwavelength waveguide," *Photon. Res.*, vol. 6, no. 1, pp. 18–23, 2018.
- [31] M. Yuan et al., "Curved terahertz surface plasmonic waveguide devices," *Opt. Express*, vol. 28, no. 2, pp. 1987–1998, 2020.
- [32] Y. Zhang et al., "Rotated pillars for functional integrated on-chip terahertz spoof surface-plasmon-polariton devices," *Adv. Opt. Mater.*, vol. 10, no. 11, 2022, Art. no. 2102561.
- [33] M. Yuan et al., "Ultra-compact terahertz plasmonic wavelength diplexer," *Appl. Opt.*, vol. 59, no. 33, pp. 10451–10456, 2020.
- [34] M. Yuan et al., "Terahertz spoof surface plasmonic logic gates," *iScience*, vol. 23, no. 11, 2020, Art. no. 101685.
- [35] Q. Cheng et al., "Flexibly designed spoof surface plasmon waveguide array for topological zero-mode realization," *Opt. Express*, vol. 26, no. 24, pp. 31636–31647, 2018.
- [36] T. Chen et al., "Distinguishing the topological zero mode and tamm mode in a microwave waveguide array," *Annalen der Physik*, vol. 531, no. 12, 2019, Art. no. 1900347.
- [37] W. Song et al., "Breakup and recovery of topological zero modes in finite non-Hermitian optical lattices," *Phys. Rev. Lett.*, vol. 123, no. 16, 2019, Art. no. 165701.
- [38] W. Song et al., "Robust and broadband optical coupling by topological waveguide arrays," *Laser Photon. Rev.*, vol. 14, no. 2, 2020, Art. no. 1900193.
- [39] A. J. Heeger, S. Kivelson, J. R. Schrieffer, and W.-P. Su, "Solitons in conducting polymers," *Rev. Modern Phys.*, vol. 60, no. 3, 1988, Art. no. 781.
- [40] X. Shen and T. J. Cui, "Planar plasmonic metamaterial on a thin film with nearly zero thickness," *Appl. Phys. Lett.*, vol. 102, no. 21, 2013, Art. no. 211909.
- [41] X. Zhang et al., "Terahertz surface plasmonic waves: A review," *Adv. Photon.*, vol. 2, no. 1, 2020, Art. no. 014001.
- [42] M. Yuan et al., "High-performance and compact broadband terahertz plasmonic waveguide intersection," *Nanophotonics*, vol. 8, no. 10, pp. 1811–1819, 2019.
- [43] L. Chen et al., "Defect-induced fano resonances in corrugated plasmonic metamaterials," *Adv. Opt. Mater.*, vol. 5, no. 8, 2017, Art. no. 1600960.
- [44] S. A. Maier, *Plasmonics: Fundamentals and Applications*, vol. 1. Berlin, Germany: Springer, 2007.

- [45] T. W. Ebbesen, H. J. Lezec, H. F. Ghaemi, T. Thio, and P. A. Wolff, "Extraordinary optical transmission through sub-wavelength hole arrays," *Nature*, vol. 391, no. 6668, pp. 667–669, 1998.
- [46] See Supplemental Material for a detailed description of bends and passive routing structures, the SSH model for the domino waveguide dimer chains in one dimension, the robustness of the antikink structure with respect to dimer number N , the number of waveguide array, the role of periodic structure for propagation x -direction, performances of various THz waveguides, and Supplemental Figures.
- [47] X. Zang et al., "Metasurface for multi-channel terahertz beam splitters and polarization rotators," *Appl. Phys. Lett.*, vol. 112, no. 17, 2018, Art. no. 171111.
- [48] X. Zang et al., "Manipulating terahertz plasmonic vortex based on geometric and dynamic phase," *Adv. Opt. Mater.*, vol. 7, no. 3, 2019, Art. no. 1801328.
- [49] B. Yao et al., "Dual-layered metasurfaces for asymmetric focusing," *Photon. Res.*, vol. 8, no. 6, pp. 830–843, 2020.



Pan Hu is currently working toward the M.S. degree in electronic information with the University of Shanghai for Science and Technology, Shanghai, China.

His research interests include terahertz silicon photonic devices, plasmonics, and topological photonics.



Lin Chen (Member, IEEE) received the B.S. and M.S. degrees in electrical engineering from Southeast University, Nanjing, China, in 2002 and 2005, respectively, and the Ph.D. degree in optics from Shanghai Jiao Tong University, Shanghai, China, in 2008.

From 2007 to 2008, he was at Avanex Corporation as a Senior Engineer. From 2012 to 2013, he was a Visiting Scholar at State Key Laboratory of Millimeter Waves, Southeast University. From 2015 to 2016, he was a Visiting Researcher at Ultrafast THz

Optoelectronic Laboratory, Oklahoma State University, Stillwater, OK, USA. He was designated Shanghai "Dawn Scholar," "Chengguang Scholar," "Top-Notch Young Talents," "Rising-Star," "Pujiang Talent," and other talent titles. He has authored or coauthored more than 70 peer reviewed papers with more than 2000 citations and H-index 26 (including 4 Highly Cited Paper) in Science Citation Indexed journal, such as *Light: Science and Applications*. He has also applied for more than 40 invention patents, 21 authorized, and 1 U.S. patent.

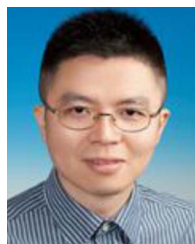
Dr. Chen was a recipient of Publons Peer Review Award in 2018 and 2019. As the first person in charge, he has undertaken a number of national level projects, including the National Key R&D Plan "Major Scientific Instrument and Equipment Development" (Chief Scientist), Two National Major Instrument Projects (project), National Natural Foundation of China (General and Youth), and several projects in Shanghai. He is currently the Editorial Board Member of *Frontiers in Physics*, Guest Editor and Corresponding Expert for *Frontiers of Information Technology and Electronic Engineering*.



Alexander Pavlovich Shkurinov received the master's, Ph.D., and Doctor (Habilitation) degrees in physics and math sciences from M.V. Lomonosov Moscow State University, Moscow, Russia, in 1985, 1988, and 2013, respectively.

Since 2015, he has been a Professor with the Faculty of Physics, MSU. His research interests are mainly centered around the development and application of femtosecond laser techniques, time-resolved spectroscopy of molecules in liquid phase, nonlinear optics, and THz techniques and spectroscopy. He has

authored and coauthored more than 300 papers in peer-reviewed scientific journals, and was invited to deliver more than 60 invited lectures and talks. In 2008, the Russian Optical Society awarded him with the medal in honor of Prof. Rozhdstvensky for his contribution into the development of optical science and technology.



Yiming Zhu (Senior Member, IEEE) received the B.S. and M.S. degrees in applied physics from Shanghai Jiaotong University, Shanghai, China, in 2002 and 2004, respectively, and the Ph.D. degree in electronics engineering from the University of Tokyo, Tokyo, Japan, in 2008.

He is a "Youth Science and Technology Innovation Leader" and "Young Yangtze Professor" with the University of Shanghai for Science and Technology, Shanghai, China, and currently serves as the Vice Director of the Shanghai Key Lab of Modern Optical System, Shanghai. His research focuses on terahertz technologies and applications, including terahertz devices, terahertz spectroscopy, imaging systems, terahertz bioapplications, etc. He has authored or coauthored more than 100 papers, including >40 papers in *Light Science and Applications*, *Advanced Optical Materials*, *Applied Physics Letters*, *Optics Letters*, *Optics Express*, etc. (Top 5%), including five papers are selected as ESI papers. He has been responsible for more than 20 projects at the national and ministerial/provincial levels, which include 1 project supported by the National 863 Project, 4 projects supported by the National Natural Science Foundation of China, 2 subprojects supported by the National 973 Project, 2 projects supported by the Major National Development Project of Scientific Instrument and Equipment, etc.

Dr. Zhu won the title of "New Century Talent" from the Ministry of Education in 2012. In 2013, he was appointed as a Council Member of the China Instrument and Control Society. In 2014, he won the title of "Excellent Academic Leaders of Shanghai", and was appointed as a Council Member of the China Optical Engineering Society and a member of the China Youth Scientist and Technician Association. In 2016, he was selected as "Shanghai Leading Talent" and "Young Yangtze Scholar." In 2017, he was awarded the "Outstanding Youth Foundation" by the "National Natural Science Foundation of China," and selected into "The National Key Talent Project." In 2018, he was recognized as a "Youth Science and Technology Innovation Leader" by the "Ministry of Science and Technology of China," and received the special State Council allowance. He was a recipient of the first prize of Shanghai Teaching Achievement Award. He is currently the Director of the Terahertz Spectral and Imaging Technology National Co-operative Innovation Center, the Terahertz Precision Biomedical Technology Overseas Expertise Introduction Center for Discipline Innovation, the Terahertz Technology Innovation International Joint Laboratory at University of Shanghai for Science and Technology, and Lomonosov Moscow State University.



Songlin Zhuang received the B.S. degree in physics from Fudan University, Shanghai, China, in 1962, and the Doctorate degree in electronic engineering from Pennsylvania State University, PA, USA, in 1982.

From 1962 to 1979, he worked at the Shanghai Institute of Optical Instruments. In 1979, he went to Michigan State University, USA, for visiting research. In 1983, he returned to the Shanghai Institute of Optical Instruments as the Director and Senior Engineer. From 1988 to 1992, he served as the Director

and Researcher of the Shanghai Institute of Laser Technology. Since 1995, he has been the President of the School of Optical-Electronic and Computer Engineering, University of Shanghai for Science and Technology, Shanghai, China. More than 100 kinds of optical systems and instruments have been designed. He is the first researcher to carry out optical system CAD in China. He presided over and completed the largest optical instrument design software system in China, and made original achievements in the optimization method of statistical test total extreme value and the nonlinear model of tolerance. In the field of optical image psychophysics experiment, he has carried out the first work in China. He has made a comprehensive and systematic research on incoherent optical information processing and rainbow holography, and is known as "one of the main contributors of modern white light information processing." A variety of optical methods have been proposed in the study of phase recovery of complex objects, which has opened up a new research direction in this field. The CdSe liquid crystal light valve has reached the international advanced level at that time. Outstanding achievements have been made in super-resolution optical imaging, grating diffraction vector mode theory, high-speed optical multichannel mode/number transformation, transformation optics, and artificial medium materials. Over the years, he has personally supervised more than 20 master's and doctoral students. The graduates have made a lot of contributions in the field of optical engineering at home and abroad. One of his students' doctoral dissertation was selected as the National 100 Excellent Doctoral Dissertations in 2009. The course of optical information technology that he taught has won the National Excellent Course in 2008.

Dr. Zhuang was a recipient of many ministerial-level science and technology progress awards and many honorary awards.